ACS APPLIED MATERIALS & INTERFACES

Research Article

www.acsami.org

Direct Growth of Freestanding ZnO Tetrapod Networks for Multifunctional Applications in Photocatalysis, UV Photodetection, and Gas Sensing

Yogendra Kumar Mishra,*[,†] Gaurav Modi,[†,‡] Vasilii Cretu,[§] Vasile Postica,[§] Oleg Lupan,[†,§] Tim Reimer,[†,∥] Ingo Paulowicz,[†] Viktor Hrkac,[†] Wolfgang Benecke,[⊥] Lorenz Kienle,[†] and Rainer Adelung[†]

[†]Institute for Materials Science and [∥]Technology for Silicon Based Micro- and Nanosystems, Institute for Electrical Engineering, University of Kiel, Kaiserstrasse 2, 24143 Kiel, Germany

[‡]Department of Metallurgical and Materials Engineering, Indian Institute of Technology, Roorkee 247667, India

[§]Department of Microelectronics and Biomedical Engineering, Technical University of Moldova, 168 Stefan cel Mare Boulevard, MD-2004 Chisinau, Republic of Moldova

[⊥]Fraunhofer Institute for Silicon Technologies, Fraunhoferstrasse 1, 25524 Itzehoe, Germany

Supporting Information

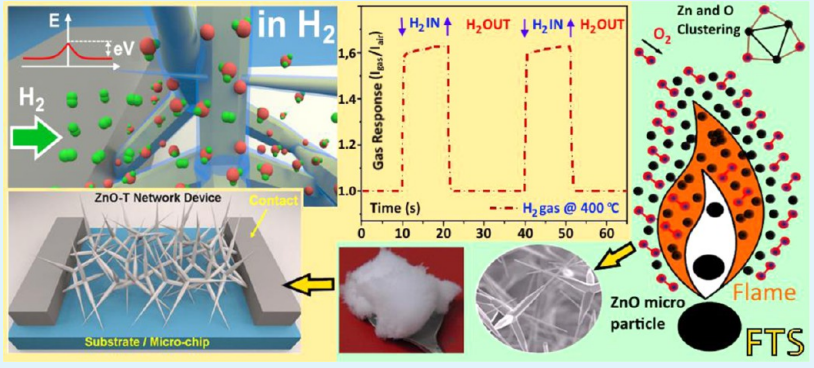

ABSTRACT: Growth of freestanding nano- and microstructures with complex morphologies is a highly desired aspect for real applications of nanoscale materials in various technologies. Zinc oxide tetrapods (ZnO-T), which exhibit three-dimensional (3D) shapes, are of major importance from a technological applications point of view, and thus efficient techniques for growth of different varieties of tetrapod-based networks are demanded. Here, we demonstrate the versatile and single-step synthesis of ZnO-T with different arm morphologies by a simple flame transport synthesis (FTS) approach, forming a network. Morphological evolutions and structural intactness of these tetrapods have been investigated in detail by scanning electron microscopy, X-ray diffraction, and micro-Raman measurements. For a deeper understanding of the crystallinity, detailed high-resolution transmission electron microscopic studies on a typical ZnO tetrapod structure are presented. The involved growth mechanism for ZnO tetrapods with various arm morphologies is discussed with respect to variations in experimental conditions. These ZnO-T have been utilized for photocatalytic degradation and nanosensing applications. The photocatalytic activities of these ZnO-T with different arm morphologies forming networks have been investigated through the photocatalytic decolorization of a methylene blue (MB) solution under UV light illumination at ambient temperature. The results show that these ZnO-T exhibit strong photocatalytic activities against MB and its complete degradation can be achieved in very short time. In another application, a prototype of nanoelectronic sensing device has been built from these ZnO-T interconnected networks and accordingly utilized for UV detection and H_2 gas sensing. The fabricated device structures showed excellent sensing behaviors for promising practical applications. The involved sensing mechanisms with respect to UV photons and H_2 gas are discussed in detail. We consider that such multifunctional nanodevices based on ZnO tetrapod interconnected networks will be of interest for various advanced applications.

KEYWORDS: *freestanding ZnO tetrapods, photocatalysis, network-based nanoelectronic device, nanoarm, UV photodetection and gas sensing*

Received: March 31, 2015
Accepted: June 8, 2015
Published: June 8, 2015

DOI: 10.1021/acsami.5b02816
ACS Appl. Mater. Interfaces 2015, 7, 14303−14316

1. INTRODUCTION

Nanoscale structures from different metal oxide materials have got significant attention in terms of synthesis strategies, characterizations, and structure−property correlations, and various remarkable milestones indeed have been established.[1,2] In fact, the current focus of the nanoresearch community is to synthesize different nanostructures in such a way that they can be easily utilized for different applications ranging from nanoelectronics to biomedical engineering. However, a simpler synthesis process for mass-scale production with cost effectiveness remains one of the major challenges at the current stage of nanotechnologies for metal oxides. Synthesis by wet chemistry involves some chemical reagents, which always raises an issue about true surface accessibility of oxide nanostructures for particular applications; however, desired synthesis and cost effectiveness are the most important factors for physical synthesis routes. Several synthesis approaches have been adopted and various types of nanostructures are already being proposed for different applications.[3−6] In order to overcome the application challenges, unconventional techniques with new approaches were introduced and they have also been quite successful.[7] Just as an example, integrating nanoscale structures into electronic devices and realization of proper electrical contacts are always critical issues, and some innovative approaches[8,9] have nicely demonstrated their potential. There are still important issues to be solved, like appropriate substrate choices, multistep processing, nanostructure growth control, and avoiding the limitation for only selected applications. It is very important to emphasize here that freestanding nanostructures from different nanomaterials could play a decisive role when it comes to their real applications in different technologies, as they can be freely utilized in the desired manner on different types of substrates. However, in most cases, freestanding nanostructures suffer from prominent issues like agglomerations and sustainability in normal ambient environments, which are mainly decided by the right size, crystallographic orientation, and the shape of the nanostructures.[9−11] Architecture of the nanostructure is an even more important factor because particular shapes, like tetrapods/multipods with long nanoarms, can prevent agglomeration (spherical and rod nanostructures probably exhibit such limitations) of the nanomaterial itself. Growth of nanostructures with branched morphologies, like tetrapods and multipods, from different materials has been a highly desirable research aspect because of their large degree of multifunctionality.[12−16] Nanostructures having appropriate length scales (still preserving nanoscale features) and three-dimensional (3D) geometry—for example, hollow sea urchins, tetrapods, multipods, branched structures, and others—exhibit a pivotal role with regard to real applications in different directions, as they can be freely handled.[17,18] Although they are technologically very relevant, these freestanding 3D shaped structures are equally difficult to grow by standard synthesis methods. Nanostructures from a few materials (with appropriate crystal structure) can acquire such 3D geometries and can only be synthesized by a certain growth process. Zinc oxide (ZnO) nanostructuring has been quite popular in this regard as nanostructures from simple to very complex can be grown, and they indeed exhibit bright application perspectives in future nanotechnology.[19−21] Inspired by the unique features of 3D nanostructural geometries and the multifunctionality of ZnO material, we demonstrate here the versatile synthesis of freestanding ZnO tetrapodal structures with different arm shapes and their potential multifunctional applications.

ZnO is a preferred choice because it belongs to a metal oxide family that has attracted wider research attention than others. This is mainly due to its interesting properties for practical applications, such as a direct and wide band gap (∼3.37 eV), high exciton binding energy (∼60 meV), UV light sensitivity, and other remarkable optical and piezoelectric properties.[2] Nano- and microstructures from ZnO have found potential applications in diverse fields including water purification and photocatalysis,[10,22−25] UV and gas sensors,[26,27] dye-sensitized solar cells,[28,29] light-emitting diodes, and significantly in biomedical engineering,[30,31] according to previous experimental reports. From the literature, it is obvious that ZnO structures can acquire almost any type of shape within our imagination, and most of them have been accordingly proposed for various applications. However, detailed/deep understanding of the involved growth mechanism with predicted growth of particular shapes of ZnO nanostructures by cost-effective synthesis techniques are still required. In this context, ZnO tetrapodal structures and their interconnected macroscopically expanding networks are of major importance from practical, scientific, and technological points of view. Here we concentrate mainly on the simple and direct growth of freestanding ZnO tetrapod-shaped structures by a novel flame transport synthesis (FTS) approach. The tetrapodal shape is quite attractive and interesting in the sense that it exhibits a 3D geometry with four arms connected together from the central core at an average angle of ∼110° with respect to each other, and the nanoscale features of their arms can still be utilized in a unique practical manner, including formation of large, highly porous, mechanically flexible networks that are stable at high temperatures. The FTS method[32] offers direct (chemical reagent-free) synthesis in large amounts of zinc oxide tetrapods (ZnO-T) with controlled shape. Due to their 3D structural integrity, the ZnO tetrapod structures do not strongly agglomerate with each other, and they can be easily separated in form of freestanding powder for desired applications.[17] Even if a certain amount of ZnO tetrapods is filled in an appropriate scaffold (e.g., ceramics cylinder) and then heated at higher temperatures (up to 1200 °C for 4 h), large interconnected networks (on approximately a cubic centimeter scale) with desired porosities and Young's modulus can be easily constructed. Such interconnected networks are currently very important materials for applications in different technologies as well as templates for growth of new types of multifunctional 3D networks.[33,34] Variations in temperature and growth duration in the FTS process result in formation of tetrapods with specific arm morphologies that can lead to different functionalities.

In the present work, ZnO tetrapods with different arm shapes forming interconnected networks have been successfully synthesized by the FTS process, and their detailed morphological and structural characterizations are shown. The multifunctionality of ZnO-T with different arm morphologies was proven by photocatalytic responses of the structures (with respect to methylene blue as the model dye) and nanosensing. Such sensor structures were fabricated in a simple manner and utilized for UV photodetection and hydrogen gas sensing. Basic mechanisms for the observed photocatalytic behavior and sensing characteristics are discussed in detail.

2. EXPERIMENTAL SECTION

2.1. Synthesis of ZnO Tetrapod Interconnected Network. The flame transport synthesis (FTS) technique[32] was utilized for growth of the tetrapod-shaped ZnO structures. For ZnO-T synthesis by the FTS approach, a 2:1 mixture of poly(vinyl butyral) (PVB) and zinc

DOI: 10.1021/acsami.5b02816
ACS Appl. Mater. Interfaces 2015, 7, 14303−14316

microparticles was filled into a ceramic crucible up to 75% of its total volume; this was heated in a simple muffle-type furnace at different time durations (30−90 min) and temperatures (900 and 950 °C). Sample sets 1, 2, and 3 correspond to ZnO-T synthesized at 900 °C with growth times of 30, 60, and 90 min, respectively, while tetrapods in sample set 4 were grown at 950 °C for 60 min. The furnace was preheated to a temperature of 450 °C and then the ceramic crucible was inserted into it. Due to the high temperature of the furnace, the sacrificial polymer PVB starts burning and the generated flame carries the Zn microparticles upward, where they are then converted into ZnO nano- and microstructures due to the high temperature of the flame. During the FTS growth process, the flame and PVB also enable local control over the amount of oxygen gas necessary for the growth process.[17,32] Formation of ZnO tetrapods with different arm morphologies and their interconnected networks have been obtained by controlled FTS approaches, especially by varying the growth temperatures and times, which suggest that these technological parameters play important roles in deciding/controlling the morphology of zinc oxide tetrapods.

2.2. Morphological and Structural Investigations of ZnO Tetrapod Interconnected Networks. The morphology of the synthesized tetrapod interconnected networks was examined by a scanning electron microscope (SEM, Zeiss, 20 kV, 20 μA). X-ray diffraction (XRD) studies were performed on a 3000 TT Seifert X-ray diffractometer unit (with 40 kV and 40 mA Cu Kα radiation with λ = 0.154 059 8 nm), and the average crystal lattice parameters have been determined by the Scherrer method from the diffraction peaks. The micro-Raman spectrometer WITec system was used in this study. A 532.2 nm line from a Nd:YAG laser at an output power of 8 mW was used as the excitation source. Light was focused onto the sample by use of an objective lens mounted on an optical microscope connected to the Raman spectrometer. A charge-coupled device (CCD) detector (Wright Instruments, Ltd.) was used and the CCD chip was maintained at −60 °C. Immediately before actual measurements, the instrument was calibrated to the same accuracy with standard silicon substrate. Structural investigations on ZnO tetrapods were performed with a FEI Tecnai F30 G^2 STwin operated at 300 kV [field emission gun (FEG), spherical aberration coefficient C_S = 1.2 mm]. Selected area electron diffraction (SAED) was carried out by using apertures limiting the illuminated area of a specimen to diameters up to 250 nm. The evaluation of all high-resolution transmission electron microscopy (HRTEM) micrographs, fast Fourier transforms (FFTs), and electron diffraction (ED) patterns were performed with the program Digital Micrograph 3.6.1 (Gatan, Inc.). Simulated SAED patterns were obtained with the JEMS program package.[35,36] Contrast enhancement for HRTEM micrographs was enabled by use of the HRTEM filter plug-in, and DigitalMicrograph scripting was applied.[37]

2.3. Photocatalytic Measurements on Different ZnO Tetrapod Networks. Photocatalytic studies on the synthesized ZnO tetrapods were performed with respect to methylene blue (MB) dye. A 1 μmol·L^{-1} solution of MB was prepared in water by withdrawing 100 μL of 1 mM stock solution through a pipet in a volumetric flask and subsequently diluting it by addition of distilled water so as to make the total volume of the solution 100 mL. A portion (60 mL) of this solution was taken in a beaker, which was mounted on a magnetic stirrer rotating at a speed of 300 rpm, and then 60 mg of as-prepared ZnO-T sample was added into it. Another identical beaker, containing the same MB solution but no ZnO-T, was used as the reference for the experiment. Both beakers were mounted on the magnetic stirrer and were irradiated with UV light from a locally made UV diode array consisting of four diodes (central wavelength = 370 nm, 170 mW/diode) for a duration of ∼10 min. Aliquots of the solution were taken at intervals of 1 min and pipetted into precision glass cuvettes, which were then analyzed by a UV−visible spectrophotometer. Before aliquots were drawn out from the beaker, the solution was allowed to stand still without any stirring for about 2 min, during which the tetrapods settled to the bottom of the beaker. After each measurement, the precision glass cuvettes were cleaned with acetone and deionized water and subsequently dried. Absorbance value of the aliquots was measured by photometry on a UV−visible spectrophotometer at a wavelength of 664 nm, for which the signal intensity was maximal. For a solution with known absorption (A), the concentration can be easily calculated by Beer−Lambert's relationship[38] $A = \varepsilon bc$, where ε is the wavelength-dependent molar absorptivity coefficient, b is the path length, and c is the concentration of the solution. By use of Beer−Lambert's relationship, normalized concentration of MB solution has been calculated at intervals of 1 min and its decolorization efficiency (η)[39] (after 10 min) was determined from eq 1:

$$\eta = \left[\frac{(C_0 - C_t)}{C_0}\right] \times 100 \quad (1)$$

where C_0 and C_t are the initial (t = 0) and final (after time t) concentrations of the MB solution.

2.4. ZnO Tetrapod Interconnected Network-Based Nanosensing Devices. For investigation of sensing performance, ZnO-T networks were annealed at 1100 °C for 1 and 4 h to make reliable interconnections between tetrapod arms and then integrated in a device structure by mounting network material between gold pads, and electrical contacts were established with silver paste on the patterned substrate. Another set of samples was made by metal deposition through a mask to obtain external electrodes (obtained results were identical to those from silver paste). Photodetection performance of tetrapod network structures toward UV radiation pulses at 365 nm was investigated as described below and in our previous works.[40,41] Another ZnO tetrapod network-based device was fabricated in a similar manner to investigate gas (H_2) sensing performance. For sensing measurements, the ZnO-T network device was placed in a measuring apparatus as demonstrated here and also in our previous work.[40]

3. RESULTS AND DISCUSSION

Morphologies of different types of ZnO tetrapods and their networks synthesized by the FTS approach were investigated in detail by SEM, as shown in Figures 1 and 2. As mentioned above, in FTS experiments, the temperature and duration were changed to control the morphology of the ZnO-T nanoarms. In sample set 1, grown at 900 °C for 30 min, tetrapods consist of uniform hexagonal cylindrical arms with narrowing cylindrical hexagonal flat tips (see SEM images in Figure 1a−c). The tetrapods typically exhibit a diameter of about 3−5 μm at their base and a tip diameter of ∼1 μm. The lengths of the tetrapod arms are in the range 15−20 μm. For sample set 2, grown at 900 °C for 60 min, a distinct morphology of the tetrapods has been obtained, as presented in Figure 1d−f. It can be seen that the diameter of the tetrapod arms decreases abruptly after a certain distance from the base, resulting in a tetrapod-shaped nanoneedle structure. It is evident that the tetrapod arm can be distinctively divided into three main regions: the first segment is homogeneous in diameter, followed by a region of abrupt change in diameter, and finally ending in a needle-shaped segment. The needle-shaped segment is extraordinarily long, with lengths even reaching up to 30 μm.

SEM images corresponding to sample set 3, tetrapod networks synthesized at 900 °C for 90 min, are shown in Figure 2a−c with increasing magnification. The SEM results demonstrate that the grown tetrapods exhibit a morphology similar to that presented in Figure 1a−c. However, the main difference in this case is that the tetrapods self-assemble and form interconnections with each other, thus leading to formation of an interconnected tetrapod network. In some instances complete interpenetrations can be observed; see Figures 1a−c and 2a−c. Growth at higher temperature of about 950 °C for 60 min, that is, sample set 4, leads to a drastic change in the arm morphology of the resultant structures. Formation of multipods predominates over that of tetrapods, as shown in Figure 2d−f. The ends of the multipod arm are needlelike but not as long as those observed for sample set 2, grown at 900 °C for 60 min.

DOI: 10.1021/acsami.5b02816
ACS Appl. Mater. Interfaces 2015, 7, 14303−14316

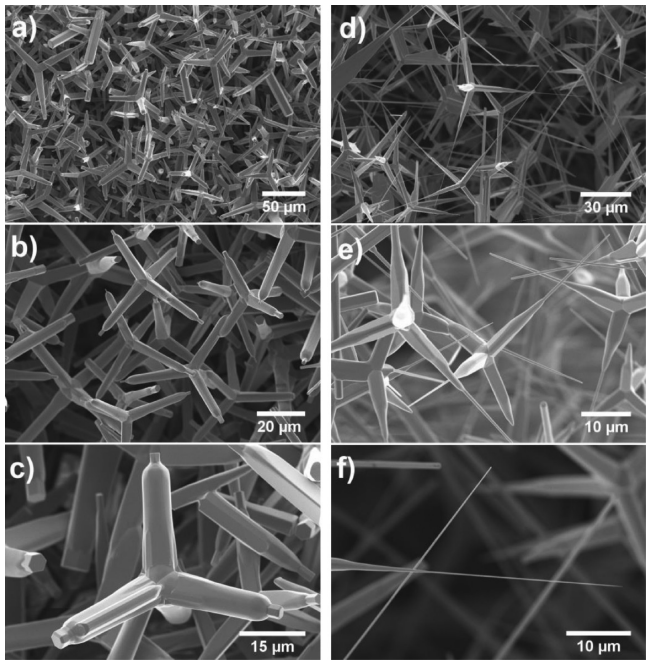

Figure 1. (a–c) SEM images (increasing magnification) of sample set 1: ZnO-T network grown at 900 °C for 30 min. (a) Dense network of uniform ZnO-T. (b) Magnified view of tetrapod network, clearly displaying the uniformity of all tetrapod arms. (c) Further magnified SEM image showing ZnO-T with uniform hexagonal cylindrical arms and a smaller cylindrical hexagonal tip on their top. (d–f) SEM images (increasing magnification) of sample set 2: ZnO-T network grown at 900 °C for 60 min. (d) 3D network of well-spaced ZnO-T with needle-shaped arms. (e) Magnified view of the tetrapod network having nanoneedle-shaped tips of their arms. (f) Further high-magnification SEM image showing the nanoscopic diameter of very long tips (up to 30 μm).

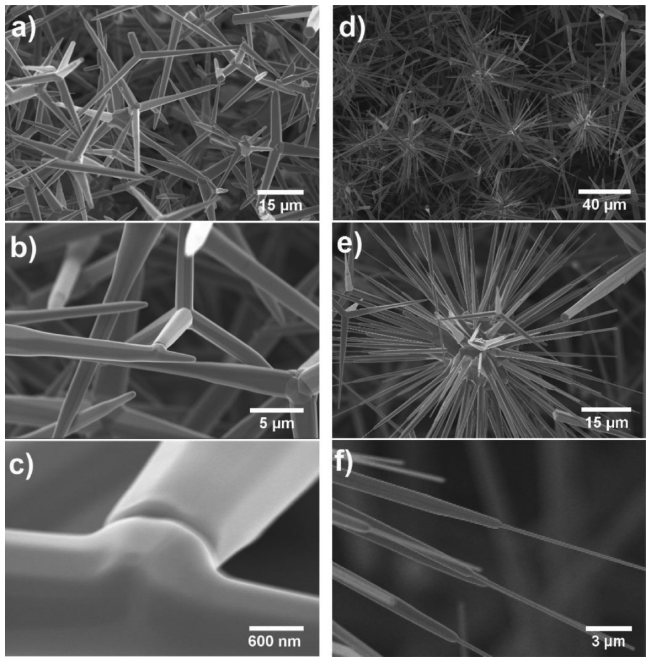

Figure 2. (a–c) SEM images (increasing magnification) of sample set 3: ZnO tetrapod networks grown at 900 °C for 90 min. (a) Low-magnification SEM image showing self-assembled network of ZnO tetrapod with many interconnections. (b) Magnified SEM image showing the morphology of tetrapod arms and formation of interconnections between them. (c) Further magnified SEM demonstrating a clear view of formed interconnections. (d–f) SEM images (increasing magnification) of multi/tetrapodal ZnO nano- and microstructures (sample set 4) grown at 950 °C for 60 min. (d) Dense network of tetrapods and multipods with multipod formation predominating over tetrapods. (e) Magnified view of a single multipod with needlelike tips. (f) Further high-magnification view of the tips of the multipod.

As mentioned above, the morphology of the nano- and microstructures plays a very important role in their chemophysical properties, while the growth technique has a strong influence on the properties too.[17] ZnO nanostructures have been fabricated via different methods, with vapor transport process being the most common: it involves a reaction between zinc vapor and oxygen gas, giving rise to ZnO nanostructures.[42] The Zn vapor and oxygen gas can be supplied via different routes, such as thermal decomposition of ZnO or direct heating of Zn micropowder under controlled flow of O_2. The carbothermal method has also been a very popular route of synthesizing ZnO nanostructures, in which ZnO is reduced (in Zn and O vapors) with the help of graphite at higher temperatures (from 800 to 1100 °C), followed by reaction with O_2 under controlled conditions.[43] Vapor–liquid–solid (VLS) growth is probably the most versatile process and has been adopted for the synthesis of one-dimensional (1D) ZnO structures like nanorods, nanowires, and nanotrees.[44] The developed FTS method in the present paper also belongs to the category of vapor transport process, but it requires only precursor metal microparticles (Zn) and sacrificial polymer (PVB, a completely decomposable polymer, thus considered a green polymer) and it offers direct growth (i.e., not involving any chemical reagents) of ZnO tetrapods in a single-step process. Different varieties of ZnO tetrapods have been successfully synthesized by proposed techniques and accordingly investigated for different applications; however, understanding the involved growth mechanism of these complex ZnO structures like tetrapods, multipods, and nanotrees is still an open issue, and it is discussed in detail here.

In order to understand the growth mechanism of these complex shaped ZnO structures, knowledge from basic crystal structure and thermodynamics is quite important. ZnO basically has three types of fast growth directions: (i) $\langle 2\bar{1}\bar{1}0\rangle$ ($\pm[2\bar{1}\bar{1}0]$, $\pm[\bar{1}2\bar{1}0]$, $\pm[\bar{1}\bar{1}20]$); (ii) $\langle 0\bar{1}10\rangle$ ($\pm[0\bar{1}10]$, $\pm[10\bar{1}0]$, $\pm[\bar{1}100]$); and (iii) $\pm[0001]$.[2] The crystal growth speed along different directions is observed to follow the order $V_{\langle 0001\rangle} > V_{\langle 01\bar{1}0\rangle} > V_{\langle 000\bar{1}\rangle}$.[45] By varying the experimental growth conditions, one can modify the relative activities of these growth facets and can thereby achieve faster growth rates along a particular direction while inhibiting the growth rate in other directions.[2] A detailed understanding of the underlying growth mechanism will allow one to synthesize diverse and complex ZnO structures like nanorods, nanowires, nanoflowers, nanocombs, nanobelts, nanosprings, nanodisks, tetrapods, and a range of other nano- and microstructures,[2,46,47] but the main emphasis here is to understand the growth mechanism of tetrapods in general and different arm morphologies in particular. The growth mechanism of ZnO-T via vapor transport process (in the FTS approach) is discussed in detail for the first time here, with consideration of the roles of different experimental parameters.

The growth of tetrapod structures and formation of different arm morphologies can be understood on the basis of variation in zinc and oxygen vapor pressures during the respective processes with their specific growth temperature.[48] Unlike the one-dimensional (1D) ZnO structures, which are normally grown by the vapor–liquid–solid (VLS) process,[44] tetrapods are believed

DOI: 10.1021/acsami.5b02816
ACS Appl. Mater. Interfaces 2015, 7, 14303–14316

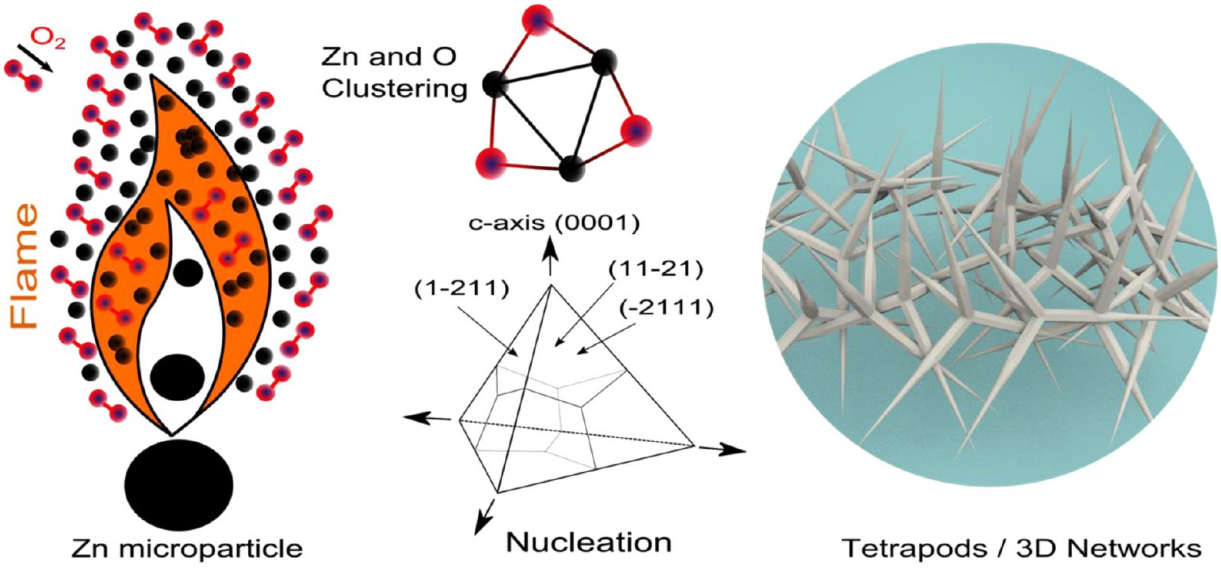

Figure 3. Growth mechanism of ZnO tetrapods and their 3D networks in the flame transport synthesis approach. The flame (generated due to the burning of sacrificial polymer PVB) carries the Zn microparticles upward, where they are subsequently transformed into the vapor state in the form of individual Zn atoms, Zn dimers, Zn trimers, etc. The highly unstable atomic variants in the Zn vapor immediately start participating in nucleation and growth processes with the help of available native oxygen molecules in the environment. First Zn and O combine to form a primary cluster, and then further available Zn and O atoms combine with this clusters at different facets to form a stable nucleus. Once the stable nucleus has been formed, further available Zn and O atoms contribute to conventional 1D spike growth along the *c*-axis (0001). Nucleation is a very crucial step: homogeneous nucleation mainly results in growth of tetrapod-type structures, however, heterogeneous nucleation could lead to growth of various morphologies, such as multipods, flowers, trees, etc. The morphology of tetrapod arms (length, thickness, shape) can be controlled by experimental conditions, and the grown tetrapods (in the form of freestanding powder or 3D interconnected network) can be accordingly utilized for desired experiments.

to form by the vapor−solid (VS) mechanism since they do not require any catalyst particles to initiate their growth.[49] During the VS process, in the higher-temperature regions, Zn vapor is formed from Zn microparticles (Figure 3), which then moves toward lower-temperature regions and participates in the nucleation process with the help of oxygen to form the ZnO core nucleus for growth of ZnO-T. Shiojiri and Kaito[50] suggested the formation of a zinc blende (ZB) core for tetrapod growth. The ⟨111⟩ directions of ZB structure exhibit a crystallographic polarity, consisting of oxygen atoms on four of the {111} ZB planes and Zn atoms on the remaining four. These planes, consisting of the Zn atoms, are more strained and consequently are the surfaces of higher energy. Thus, crystal growth occurs at a faster rate along the ⟨111⟩ directions perpendicular to Zn {111} surfaces. Wurtzite-type structured ZnO arms grow on the four {111} planes of the ZB-type core by the introduction of stacking faults, which lead to growth of tetrapod-shaped structures. In another growth model, Nishio et al.[51] figured out that the initial growth conditions favor the formation of a ZB-type nucleus, which later transforms into a more stable wurtzite-type structure. This phase transformation is believed to occur by phenomena of successive slipping along any of the three $\langle 11\bar{2}\rangle$ directions on the +{111} surfaces. A growth model named the octa-twin model has been proposed by Takeuchi et al.,[52] and they speculated that, in the initial stages of the growth process, nucleation of octa-twins (composed of eight tetrahedral crystals) takes place. These tetrahedral crystals consist of three $\{11\bar{2}2\}$ planes and a {0001} plane. The eight crystals are joined along their $\{11\bar{2}2\}$ planes leaving their {0001} planes exposed. It was assumed that the twins are of inversion type, which is antisymmetric about the twin plane. The angle between any two $\{11\bar{2}2\}$ planes is about 85.5° due to which a misfit strain exists in the octa-twin. This stored misfit strain energy is released by decohesions along the twin boundaries and the formed cracks are filled up in the subsequent growth process. Thus, the inversion-type octahedral twin finally consists of alternating (0001) and $(000\bar{1})$ planes with four surfaces of each type. Preferential growth occurs along the +*c* direction perpendicular to four of the {0001} surfaces and the octa-twins finally evolve into tetrapod-shaped architecture. This model accurately predicts the interarm angles of the tetrapod, unlike the model proposed by Shiojiri and Kaito.[50] Direct evidence for the existence of a octa-twin nucleus has also been provided in subsequent works by Dai et al.[53] through HRTEM observations. The octa-twin model has recently been revised by Ronning et al.,[54] who proposed the formation of a distorted tetrahedral wurtzite-type ZnO core made of four hexagonal ZnO grains and containing a large number of defects that relax the misfit stresses. Both the octa-twin model and the assumption by Ronning et al.[54] remain the most convincing up to now in explaining the structure and growth mechanism of ZnO tetrapods. In spite of the numerous growth models, the morphology and crystal structure of the central core in ZnO tetrapods has still remained a topic of debate.[50,51,54,55]

Once nucleation of the central core is over, the morphology of the tetrapod arms is mainly controlled by growth conditions, particularly the Zn and O vapor pressures.[48] With maintenance of identical vapor pressure (Zn and O) conditions (for example, use of external gas flow controls), growth of ZnO tetrapods with uniform arm morphologies is most likely expected; however, in the present FTS process (inside a muffle-type furnace in ambient atmosphere), the vapor pressure conditions are different (Zn vapor level is higher in the beginning of the growth process and O vapor pressure is dominant in the later stages), and this is most likely responsible for growth of ZnO-T with different arm morphologies. According to SEM results (Figures 1 and 2), one can suggest that by varying temperature and duration, growth of ZnO tetrapods with (i) nearly hexagonal, (ii) partially hexagonal, and (iii) hexagonal base with sharp needle types of arms, as well

DOI: 10.1021/acsami.5b02816
ACS Appl. Mater. Interfaces 2015, 7, 14303−14316

as ZnO multipods, has been observed. In the initial stages of growth, the O_2 vapor pressure is low because a significant amount of O_2 is used up for burning of the PVB polymer. On account of this, growth of the ZnO crystal is slower and conditions almost close to thermodynamic equilibrium exist.[56] In this situation, growth occurs along the crystallographic directions in such a way that uniform (nearly) hexagonal cylindrical arms are formed (Figure 1a−c). Another possibility could be that several ZnO nanowires initially grow from the central core and subsequent overgrowth leads to the formation of such arm morphologies (SEM studies suggest this effect). After a certain time (for longer growth duration), the ratio (Zn/O) of vapors alters (because of fixed amount of Zn precursor material and lower oxygen consumption by sacrificial polymer), thus leading to changes in the existing equilibrium conditions. The availability of higher oxygen vapor pressure in the later stage leads to modified growth kinetics of ZnO arms. The Zn vapor pressure starts decreasing with time as more and more Zn vapor is converted to solid via the VS growth mechanism, and the source of the Zn vapor is also exhausted. These conditions of increased oxygen vapor pressure and decreased zinc vapor pressure accelerate growth along the [0001] direction while it is suppressed in the other six symmetric directions of $\langle 10\bar{1}0\rangle$.[48] The formation of ZnO tetrapods (SEM images in Figure 1d−f) with arms that are hexagonal at the base with sharp needle tips could be mainly due to modifications in vapor pressure conditions in the beginning and later stages of growth, respectively.

Regarding the proposed growth mechanism of ZnO tetrapods, we point out that the morphology of sample set 1, with tetrapods grown at 900 °C for 30 min, which was the shortest growth time, is almost in agreement with our hypothesis that kinetic equilibrium conditions exist at the initial stages of growth, giving rise to uniform hexagonal cylindrical arms. The smaller-diameter hexagonal cylindrical tips of the arms are indicative that equilibrium growth conditions had changed, favoring growth along the [0001] direction and lower growth rate along the other directions. The morphology of sample set 2 (tetrapods grown at 900 °C for 60 min), exhibiting a uniform diameter of tetrapod arm up to some length and then converging away to form needlelike tips, can be preliminarily understood on the basis of our hypothesis, but only high-temperature in situ experiments will provide a definite answer about the involved process. A possible explanation could be that the length up to which the diameter is uniform corresponds to the time until which equilibrium conditions existed in the furnace. After this time, the relative increase in oxygen vapor pressure led to needle-shaped growth as discussed above. The shape of tetrapod arms for sample set 3 is also in agreement with the same hypothesis. Besides this, in sample set 3, tetrapods are also observed to form interconnections in an attempt to minimize their surface energies.[32] At higher temperatures, formation of multipods also occurs along with tetrapods, and Zheng et al.[48] demonstrated that growth of such structures mainly depends on experimental parameters like temperature and vapor pressures. It is necessary to mention here that in the present FTS process, the burning of sacrificial polymer (PVB) also plays an important role. Its decomposition temperature is around ∼400 °C; however, a degradation-resistant carbonaceous species remains until ∼700 °C.[57] At temperatures beyond 850 °C, these carbonaceous residues react with water vapor (from ambient atmosphere) and form carbon monoxide (CO) and carbon dioxide (CO_2).[57] According to the Boudouard reaction, at higher temperatures of ∼900 °C (normal temperatures in present FTS growth), a high fraction of CO molecules (>90%) is more stable in comparison to CO_2 molecules[58] and this, too, has an impact on the growth conditions of ZnO structures. Therefore, in the FTS growth process (using PVB), C, CO, and CO_2 are competing species (local controls) as they can consume free oxygen as well as can deliver the oxygen to Zn atoms. In such a case, the formation of tetrapods from Zn microparticles by use of PVB in air at ∼900 °C can be speculated via the following set of reactions (eqs 2−8):

$$\mathrm{Zn(s)} \leftrightarrow \mathrm{Zn(g)} \tag{2}$$

$$\mathrm{C(s)} + \mathrm{O_2} \leftrightarrow \mathrm{CO_2(g)} \tag{3}$$

$$\mathrm{CO_2(g)} + \mathrm{C} \leftrightarrow 2\mathrm{CO(g)} \tag{4}$$

$$\mathrm{CO_2(g)} + \mathrm{Zn(g)} \leftrightarrow \mathrm{ZnO} + \mathrm{CO(g)} \tag{5}$$

$$\mathrm{CO(g)} + \mathrm{Zn(g)} \leftrightarrow \mathrm{ZnO} + \mathrm{C(s)} \tag{6}$$

$$\mathrm{Zn(g)} + \mathrm{O_2(g)} \leftrightarrow \mathrm{ZnO(g)} \tag{7}$$

$$\mathrm{ZnO(g)} \leftrightarrow \mathrm{ZnO(s)} \tag{8}$$

The Clausius−Clapeyron relationship[59] gives the temperature dependence of Zn vapor pressure:

$$\frac{\mathrm{d}P}{\mathrm{d}T} = \frac{\Delta S}{\Delta V} \tag{9}$$

where ΔS and ΔV are changes in the specific entropy and the specific volume, respectively. A transformation from solid phase to vapor phase is associated with an increase in the volume (ΔV) and randomness (ΔS) of the system. Consequently, the ΔS and ΔV terms are both positive for the reaction Zn(s) ↔ Zn(g). This makes $\mathrm{d}P/\mathrm{d}T > 0$ (eq 9), which means that Zn vapor pressure increases with rising temperature. The situation of higher zinc and lesser oxygen (due to PVB burning) vapor pressures (at higher temperatures, >900 °C) results in the abrupt formation polyhedral ZnO seed nuclei.[44,48] The agglomeration occurs in such a way that the lower surface energy facets of the nuclei remain exposed so that the surface energy is minimized. Further growth on these low-energy facets could give rise to a multipodal structure.[48] Because such nuclei will require more energy than the growth of tetrapod arms from the facets of individual nuclei, this might be possible only at higher temperatures. But it could be another reason for growth of multipodal ZnO structures (as observed here) directly from microscale Zn particles. During rapid heating to higher temperatures (>900 °C), the Zn microparticle can undergo blast conditions (due to pressure differences between outside and inner cores), and the multiple facets of irregular fragments (microscale) after the blast act as nucleation centers for the growth of 1D ZnO spikes under described needle growth conditions. Similar to tetrapod growth, the formation mechanism of core nucleus for multipodal ZnO structures requires further attention.

In order to investigate the crystalline structure, XRD measurements of the FTS-grown ZnO tetrapods were performed. Typical XRD patterns from ZnO-T networks (sample sets 1−4) are shown in Figure 4a; the main XRD peaks are (100), (002), and (101). XRD measurements at different sample locations in each set and on several sets have been performed, and all of them exhibit almost identical XRD patterns. The XRD peaks reveal that the synthesized ZnO nano- and microtetrapods are of high crystalline quality. The lattice parameter $d(002)$ in the unstressed ZnO bulk is about 2.602 Å. However, the calculated values of

DOI: 10.1021/acsami.5b02816
ACS Appl. Mater. Interfaces 2015, 7, 14303−14316

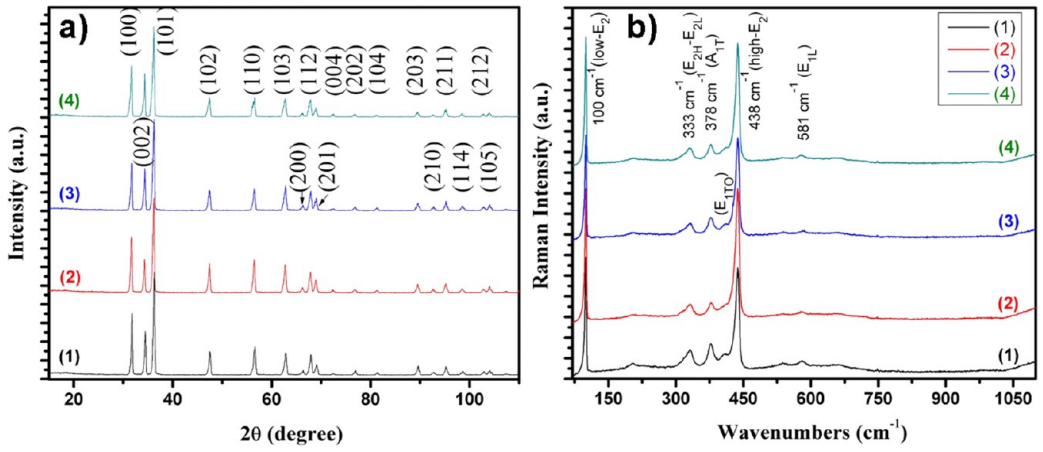

Figure 4. (a) X-ray diffraction spectra from ZnO tetrapods forming 3D networks. (b) Micro-Raman spectra of pure ZnO tetrapods on Si substrates. Four different spectra are numbered in accordance with sample set number.

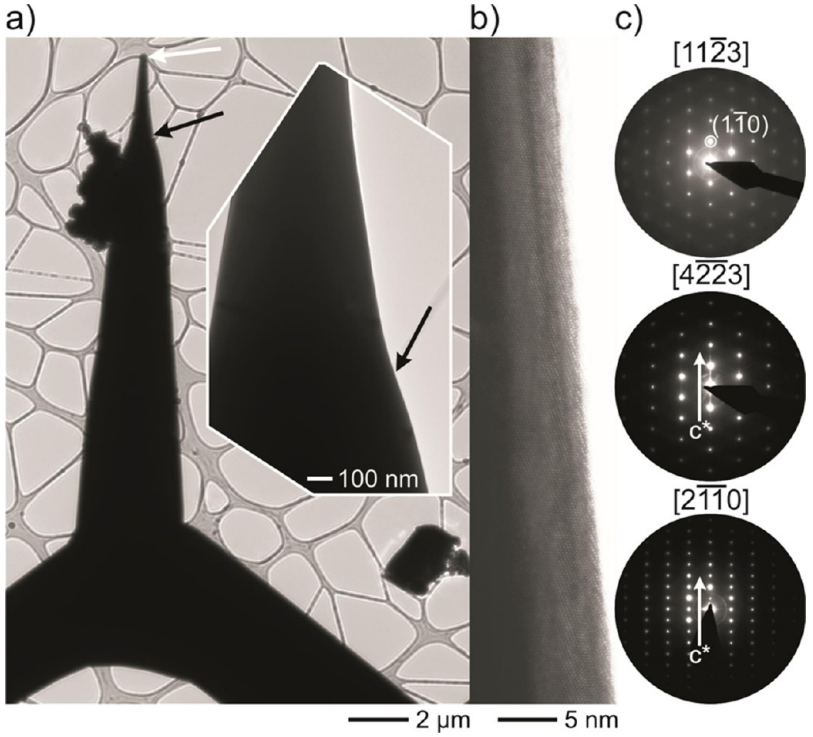

Figure 5. TEM investigations on ZnO tetrapods. (a) Bright-field image: the white arrow marks the position of HRTEM studies presented in Figure 6, while the black arrow marks the position of the magnified view depicted in the inset. The arrow in the inset marks the position of the HRTEM micrograph (panel b) oriented along the [11$\bar{2}$3] zone axis. (c) SAED tilting series for different zone axes. The growing direction of a single tetrapod crystal is along the *c*-axis.

lattice parameters are about 2.601, 2.608, 2.606, and 2.607 Å for synthesized ZnO structures of sample sets 1−4, respectively. It confirms their high crystalline nature and indicates a low strain level that exists in the ZnO tetrapods. In order to investigate the influence of growing regimes on the micro-Raman scattering in ZnO nano- and microstructures, room-temperature Raman measurements on all four sample sets were performed, and the corresponding spectra are shown in Figure 4b. In wurtzite ZnO, the number of atoms per unit cell is four, so the number of phonon modes is 12. According to group theory, $\Gamma_{opt} = A_1(z) + 2B_1 + E_1(x, y) + 2E_2$, where *x*, *y*, and *z* represent the polarization directions.[60] The A_1 and E_1 modes are IR-active, polar, and split into transverse optical (TO) and longitudinal optical (LO) branches with different frequencies.[60] The E_2 modes are Raman-active only, and the B_1 modes are IR- and Raman-inactive or silent modes.[60] Figure 4b shows the micro-Raman spectrum of ZnO material with spectra of the four samples for comparison. They are clearly indicative of good wurtzite structure of pure and undoped ZnO material. No Raman peaks of Zn appeared in the spectra of ZnO nano- and microstructures, which is consistent with the XRD results. The lower-frequency low-E_2 mode in ZnO is associated with the vibration of heavy Zn sublattice, and the higher-frequency high-E_2 mode involves only the oxygen atoms.[60] The high-E_2 mode is characteristic of the wurtzite-phase

DOI: 10.1021/acsami.5b02816
ACS Appl. Mater. Interfaces 2015, 7, 14303−14316

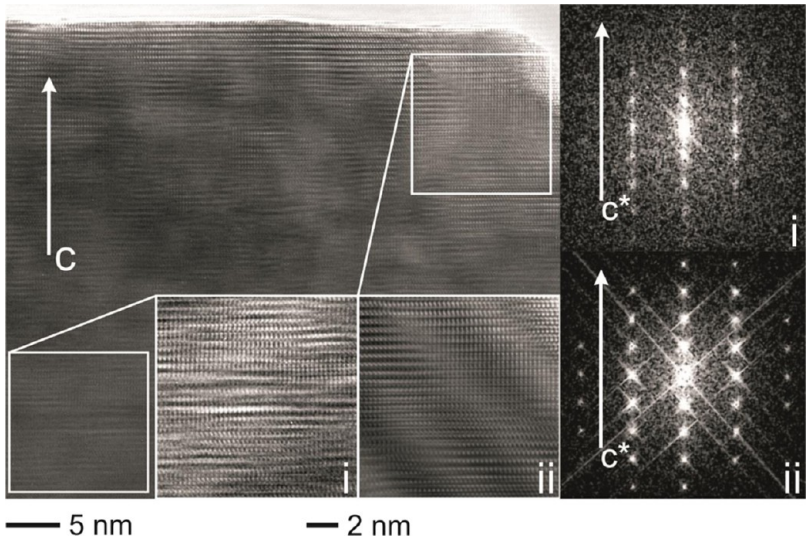

Figure 6. HRTEM micrograph of a tetrapod tip region, marked with a white arrow in Figure 5. The structure is oriented along the [2$\bar{1}$10] zone axis. Insets: (i) planar defects; (ii) defect-free. (Right panels) Corresponding Fourier transforms of the areas in the insets.

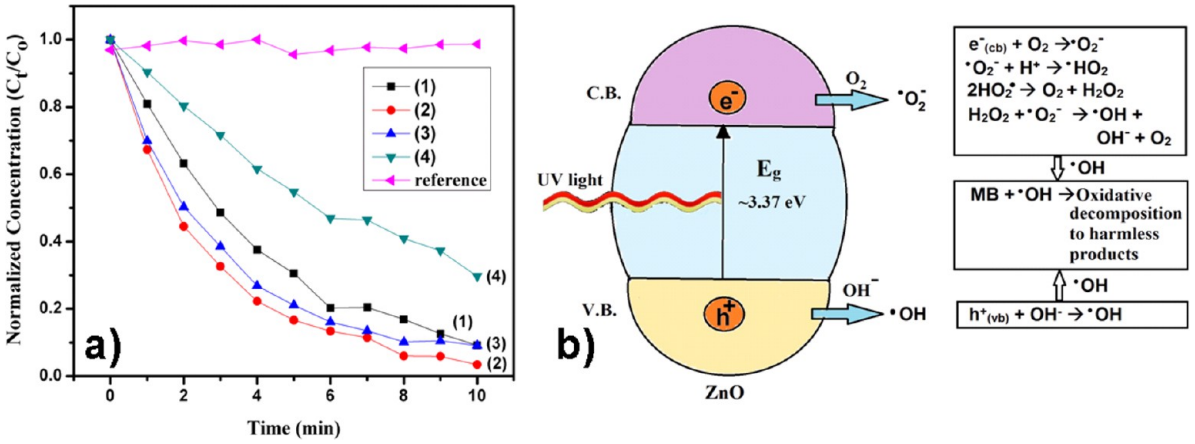

Figure 7. (a) Photocatalytic degradation of methylene blue solution as a function of irradiation time for tetrapod structures fabricated under varied technological growth conditions. (b) Schematic representation of possible photocatalytic mechanism of MB by ZnO-T networks.

material.[61] It is clearly seen that the intensities of both peaks are almost the same; however, the high-E_2 mode (438 cm^{-1}), which involves only the oxygen atoms, is slightly lower.

The intense peak near 438 cm^{-1} due to the high-E_2 mode (Figure 4b) displays clear asymmetry toward low frequencies. The asymmetric line shape has been analyzed previously in detail.[61] It could be successfully explained in terms of resonant anharmonic interaction of the high-E_2 mode with a band of combined transverse and longitudinal acoustic modes, as the steep variation of the two-phonon density of states around the high-E_2 frequency leads to a distorted phonon line shape.[60] The peak at 378 cm^{-1} corresponds to A_1(TO) mode and the broad peak at (333 cm^{-1}) to multiple-phonon scattering processes. The peak at 411 cm^{-1} corresponds to E_1(TO) mode. All Raman spectra demonstrate excellent agreement with a reference ZnO sample, emphasizing the wurtzite-type structure for all tetrapodal structures.[60]

The macroscopic investigations were further supported by structural studies at the nanoscale, as depicted in Figure 5a. The growth direction of each individual crystal of the tetrapods is along the [0001] direction; see Figure S1 in Supporting Information. High-resolution studies of the tetrapods exhibit a direct transition from the relatively thick main element of the individual crystals to their narrowing tip regions without the presence of grain or domain boundaries (see Figure 5b). Correlated electron diffraction tilting series (Figure 5c; extended tilting series presented in Figure S2 in Supporting Information) support these findings. The highly crystalline wurtzite-type fundamental structure is frequently distorted by prominent disordering of the (0001) layered structural motifs. The disordering, which is known to be based, for example, on stacking faults,[62] is indicated by diffuse intensity streaks running parallel to [0001]* inside electron diffraction patterns (Figure 5c) and Fourier transforms calculated from square selected areas of HRTEM micrographs (Figure 6). The significance of the diffuse intensity varies depending on the density of the planar defects (cf. comparison of FFTs in Figure 6).

Photocatalytic activity (PCA) of the tetrapods was investigated by degradation of 1 $\mu mol \cdot L^{-1}$ methylene blue solution under UV light irradiation for 10 min. Furthermore, a reference solution of methylene blue having no photocatalyst was prepared. Photocatalytic activity of the four different tetrapod structures and control solution is presented in Figure 7a. Sample sets 1, 2, and 3 depict significantly high PCA with almost

DOI: 10.1021/acsami.5b02816
ACS Appl. Mater. Interfaces 2015, 7, 14303−14316

complete degradation of the methylene blue solution in a time span of 10 min. Sample set 2, with tetrapods having needle-shaped tips, exhibits the highest photocatalytic activity with a decolorization efficiency of more than 95%. The obtained decolorization efficiencies (η) corresponding to sample sets 1−4 are in the following order (eq 10):

$$\eta_2\ (96\%) > \eta_3\ (91\%) > \eta_1\ (88\%) > \eta_4\ (70\%) \quad (10)$$

The reference displays only a minor change in the concentration of the MB solution, indicating that negligible degradation of the dye occurs by the influence of UV light only, without ZnO tetrapods. Sample set 3 is observed to cause greater photocatalytic degradation of the MB solution than sample set 1 up to 9 min, after which their photocatalytic efficiency is observed to approach a common value. An understanding of the possible mechanism of photocatalysis would help to better explain the observed photocatalytic degradation behavior. A photocatalyst is activated upon irradiation with a light source whose photon energy is greater than its band gap energy.[63] If such a photon is absorbed by a ZnO photocatalyst, it promotes an electron from the valence band to the conduction band and generates an electron−hole pair. These electrons and holes migrate to the surface of the photocatalyst and initiate a complex series of oxidation and reduction reactions,[64] with the dye absorbed on the surface of the photocatalyst as shown by the schematic in Figure 7b. The holes are taken up by surface hydroxyl groups, and strongly oxidizing hydroxyl radicals are produced. The superoxide radical combines with the aqueous solution and ultimately generates hydroxyl radicals. The hydroxyl radicals (OH*) cause the oxidation of the MB dye absorbed on the surface of ZnO, resulting in the formation of less harmful sulfate, ammonium, and nitrate ions and carbon dioxide gas.

It is known that the photocatalytic activity of ZnO structures significantly depends on factors such as morphology and effective surface area.[65,66] An attempt has been made next to study the variation in the photocatalytic activity of ZnO tetrapods with respect to change in their morphologies. It has been reported that ZnO tetrapods exhibit better photocatalytic activity[67] in comparison to other types of structures such as spherical ZnO nanoparticles, conventional ZnO powder, or others, but variation in the photocatalytic activities with respect to different morphologies of zinc oxide tetrapods itself was very hard to find, to the best of our literature knowledge. The observed photocatalytic behavior can be explained on the basis of the morphology of the tetrapods. Due to their three-dimensional complex structural morphology, ZnO-T do not agglomerate in the solution, which makes such networks unique and superior with respect to other nanostructures. This accounts for a very large effective surface area of the dye in contact with the ZnO. The large surface area increases dye absorption on the surface of the tetrapods and also brings about an increase in the fraction of UV light absorbed by these nano- and microstructures.[68] Hence a larger effective surface area results in higher photocatalytic activity of T-ZnO networks. Another reason for high photocatalytic activity of the tetrapods is the oxygen defects present at their surface.[69] The oxygen defects act as electron capture centers, which delay the electron−hole recombination phenomena and enhance the photocatalytic activity. The size and shape of the tetrapods affect their surface-to-volume ratio, influencing their PCA. Sample set 2 tetrapods with needle-shaped tips have the highest aspect ratio for all studied samples, leading to considerable enhancement of their surface-to-volume ratio and keeping more dispersed ZnO-T in aqueous solution. This accounts for the largest PCA efficiency of the tetrapods with needle-shaped tips at the end of the ZnO-T arms. Sample set 3 consists of converging tip tetrapods, which are not as long as the needle-shaped tetrapods. Also, the arms of these tetrapods are observed to form interconnections, which make networks more stable. These two factors result in the sample set 3 tetrapods having a lesser total surface area, due to shorter arms, for photocatalysis than needle-shaped tetrapods but greater than the uniform tetrapods, which do not have any converging tips. Hence the photocatalytic activity of sample set 3 tetrapods is observed to lie between those of the sample sets 1 and 2. Sample set 4, consisting of a tetrapod/multipod mixture, is found to have the least PCA efficiency of the four sets of samples. From Figure 2e, it can be observed that multipods have a very dense alignment of arms around the central core and are also entangled with the tetrapods. We speculate that though this dense alignment may lead to a large effective surface area, it also hinders the effective absorption of UV light by the inner surfaces. This hindrance may be the reason for the lowest observed photocatalytic activity for this sample. This observation provides us with a very significant result that tetrapods present the ideal morphological structure for maximum photocatalytic efficiency due to prevention of their agglomeration in aqueous solutions. This could be done by controlling the morphology of ZnO-T, especially their arms, via the FTS process under different technological regimes as presented above.

A multifunctional device able to work as a UV photodetector and a H_2 gas sensor was fabricated on the base of the ZnO tetrapod interconnected networks. The concept of network-based devices for sensing H_2 gas and UV irradiation is important from an industrial point of view. The ZnO nano- and microtetrapods were integrated in the device structures and investigated as reported here. Figure 8a shows the schematic representation of the multifunctional device based on ZnO tetrapod networks. In the first step, the ZnO-T network material was thermally annealed in an electrical furnace at 1100 °C for 1 h; afterward it was mounted between gold pads and contacted with silver paste on a prepatterned substrate (glass with two Au pads with thickness ∼150 nm) (Figure 8a). In our experiments, two values of the distance (d) between Au pads were chosen, 100 μm and 1 mm gaps, in order to determine the optimal sensor configuration for improvement of the I_{UVON}/I_{UVOFF} ratio and rise and decay times. Figure 8b shows the current−voltage characteristic measured in the dark and under UV illumination (wavelength of 365 nm) at 300 K of the sensor structure made of ZnO tetrapod-based networks (sample set 2) with d = 100 μm. A representative current−voltage (I−V) curve, which is very important for understanding the sensing mechanism of the ZnO network device (sample set 2), shows that it exhibits quasi-linear behavior. Additionally, the I−V characteristic of the ZnO network device at room temperature (300 K) in the dark and under UV illumination (wavelength of 365 nm), shown in Figure 8b, indicates its ability for UV detection. Next, the transient characteristics only from sample set 2, with a gap between Au pads of d = 100 μm, are presented in Figure 8c,d because it presents more practical interest due to more rapid switching activities. The ZnO multifunctional device was used for UV photodetection transient measurements in air at room temperature (cf. Figure 8c). An increase in current value (I_{UVON}) of more than 2 orders of magnitude ($I_{UVON}/I_{UVOFF} \approx 584$ for d = 100 μm) has been detected for such sensors upon exposure to UV radiation with wavelength 365 nm (see Figure 8c). Also, it can be seen that, upon exposure to UV light, the current increases very fast (rise time $\tau_r \approx 40$ ms) to 90% of maximum value

DOI: 10.1021/acsami.5b02816
ACS Appl. Mater. Interfaces 2015, 7, 14303−14316

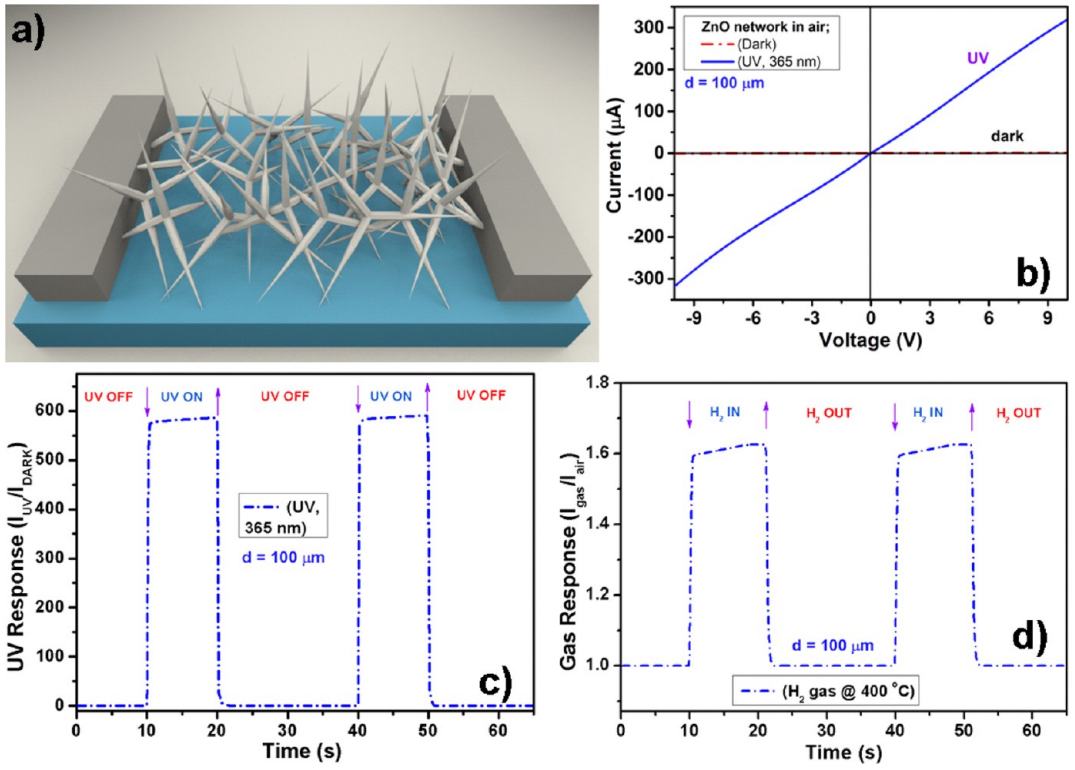

Figure 8. (a) Schematic representation of the multifunctional device based on ZnO tetrapod networks. (b) Current−voltage characteristic measured in the dark at 300 K of the sensor structure with a gap between Au pads of $d = 100$ μm, made from a ZnO tetrapod-based network (sample set 2). (c) UV photocurrent response of device toward irradiation with 365 nm light at room temperature. (d) Sensor response of device toward H_2 gas at 400 °C operating temperature and two pulses with concentrations of 100 ppm.

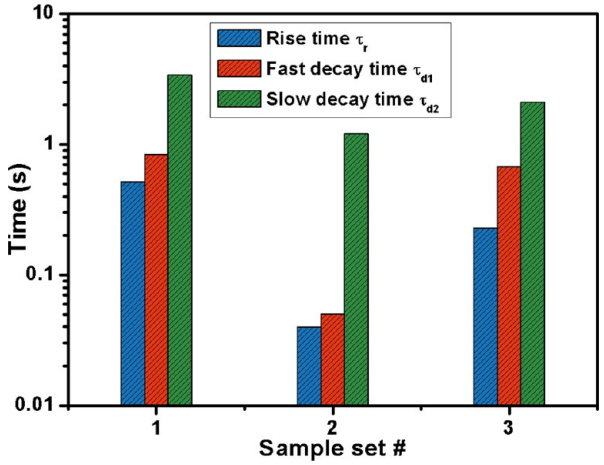

Figure 9. Rise (τ_r) and decay (fast τ_{d1} and slow τ_{d2}) times for sensor structures with a gap between Au pads of $d = 100$ μm, made from sample sets 1, 2, and 3 with ZnO tetrapod-based networks for UV response at 300 K in air.

(ON state, Figure 8c). The current decay behavior in air after the UV light is switched off (OFF state, Figure 8c) also shows a sharp decrease from 90% to 10% of the current change from I_{UVON} to I_{UVOFF}. In this decay curve we can distinguish two regions: fast decay ($\tau_{d1} \approx 50$ ms) and slow decay ($\tau_{d2} > 1.2$ s). For the sensor structures from sample set 2, with a gap between Au pads of $d = 1$ mm, the rise and decay time are comparable to those with $d = 100$ μm, taking $\tau_r \approx 40-50$ ms and $\tau_{d1} \approx 50-60$ ms for 90% of full response and recovery, respectively. Thus, the rise and decay times of the ZnO-T network-based sensor are more dependent on the morphology of the tetrapods than on the gap between gold pads. Such a fast UV response of sample set 2 is attributed to the distinct morphology and particularly to a shaped nanoneedle structure with long length (up to 30 μm), that forms more nanojunctions between tetrapod arms. As a result, more potential barriers are formed. Figure 9 presents data (Table S1, Supporting Information) on the response/recovery time from sample sets 1, 2, and 3 that confirm a faster response for sample set 2. As was previously discussed, the tetrapods from sample sets 1 and 3 exhibit similar morphology, with the main difference that tetrapods from sample set 3 possess self-assembly characteristics and form an interconnected tetrapod network. As a result, partially interpenetrated arms are formed, which directly contribute to enhancement of the UV response and improve response and recovery time values.[9] Figure 10 and Figure S3 (Supporting Information) show the current ratio ($I_{ON}/I_{OFF} \times 100$) for sensor structures with a gap between Au pads of $d = 100$ μm and 1 mm, under UV irradiation at 300 K. Sample set 2 shows a higher current ratio than other samples in both cases. For $d = 1$ mm, $I_{ON}/I_{OFF} \approx 28$; however, it is much lower than for the sensor structure with a gap of $d = 100$ μm ($I_{ON}/I_{OFF} \approx 584$). Thus, the UV response value is higly dependent on the distance between Au pads (Figure S3, Supporting Information). However, from another side, the UV response of the sensor structure with a gap between Au pads of $d = 1$ mm can be improved by annealing the ZnO-T sample at 1100 °C for a longer time. Figure S4 (Supporting Information) shows the UV photocurrent response of a device with $d = 1$ mm made of ZnO-T sample set 2 and annealed at 1100 °C for 4 h toward irradiation with 365 nm light at 300 K. In this case the response (I_{UVON}/I_{UVOFF}) value was increased from ∼28 to ∼110, due to a stronger interconnected

DOI: 10.1021/acsami.5b02816
ACS Appl. Mater. Interfaces 2015, 7, 14303−14316

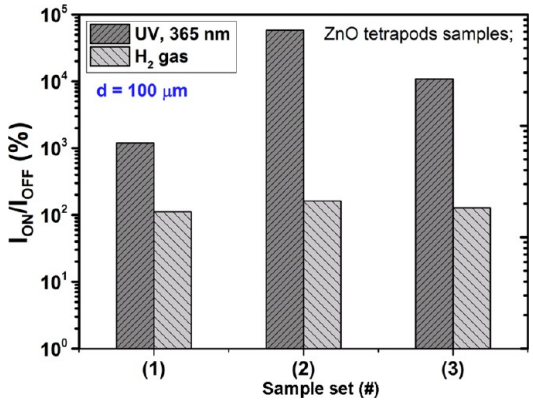

Figure 10. Current ratio ($I_{ON}/I_{OFF} \times 100$) measured from sensor structures with a gap between Au pads of $d = 100\ \mu$m (sample sets 1, 2, and 3) made from ZnO tetrapod-based 3D networks, under UV irradiation at 300 K and under H_2 gas exposure at operating temperature of 400 °C.

ZnO-T network as a result of longer annealing time (1 h versus 4 h of thermal annealing in air at 1100 °C).

Chemical sensing behavior of the device (gap between Au pads $d = 100\ \mu$m) from sample set 2 was investigated for H_2 gas under air environment (cf. Figure 8d). During H_2 gas exposure (IN condition, downward arrow in Figure 8d), a fast increase (more than ~1.62 times) of the current was detected. Upon removal of the H_2 gas (OUT condition, upward arrow in Figure 8d), a rapid step decay of the current is observable. Response rise time constants are about $\tau_r \approx 80$ ms and the decay time is about $\tau_d \approx 180$ ms. For other sample sets rise time and decay time were larger according to our experiments.

Figure 10 and Figure S3 (Supporting Information) show the current ratio ($I_{ON}/I_{OFF} \times 100$) measured from the sensor structures with a gap between Au pads of $d = 100\ \mu$m and 1 mm, respectively, made from sample sets 1, 2, and 3 with ZnO tetrapod-based networks under H_2 gas exposure at 400 °C. It can be clearly seen that sample set 2, as in the case of UV sensing, shows higher current ratio (I_{ON}/I_{OFF}) than other sample sets. In the case of sensor structure with $d = 1$ mm, the gas response ($I_{ON}/I_{OFF} \sim 1.25$) is lower than for $d = 100\ \mu$m ($I_{ON}/I_{OFF} \sim 1.62$), which is in concordance with results of UV sensing. Sample set 4 showed lower and unstable electrical characteristics and was excluded from further experiments.

The mechanism of UV detection by single tetrapods was discussed previously.[40] For our case it is schematically represented in Figure 11a,b, in the dark and under UV illumination, respectively. The space charge region (SCR) is represented by a blue shaded region, and the conduction channel is represented by a dark yellow region (Figure 11). Initially, oxygen molecules from ambient air are chemisorbed onto the surface of the zinc oxide by capturing free electrons from the tetrapods,[40,60] which creates the SCR, as demonstrated by eq 11:

$$O_{2(gas)} \rightarrow O_{2(ads)}/O_{2(ads)} + e^- \leftrightarrow O^-_{2(ads)}/O^-_{2(ads)} + e^- \leftrightarrow 2O^-_{(ads)} + e^- \leftrightarrow O^{2-}_{(ads)} \quad (11)$$

When the detector structure is illuminated with UV radiation, two processes take place. One is the generation of electron−hole pairs, which reduce the space charge region's width (Figure 11b) and enhance electrical conduction (Figure 8c). The second mechanism promotes desorption of chemisorbed oxygen species by recombination with generated holes; this process is slower,

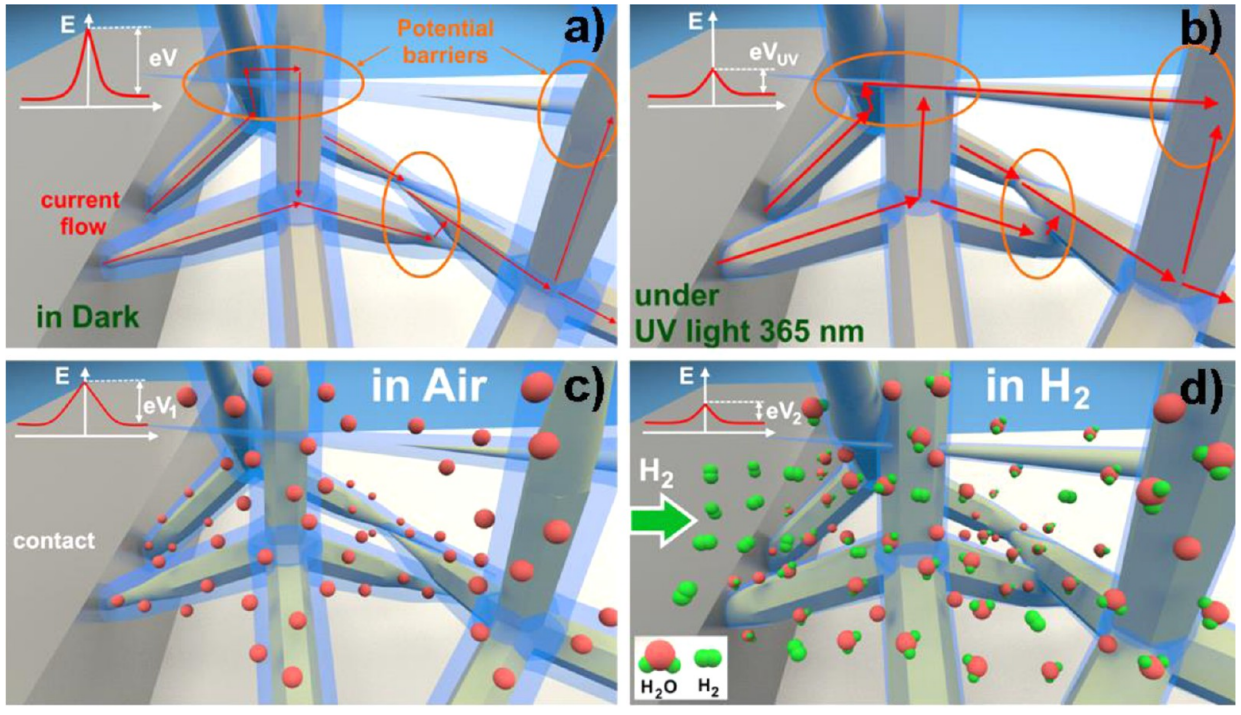

Figure 11. Schematic representation of multifunctional device operation based on ZnO tetrapod networks: (a) UV photodetector in the dark at room temperature. Depletion regions or space charge regions (SCR) are represented as more transparent zones. Conduction channels for majority charge carriers are through the middle part of tetrapods forming 3D networks. (b) UV photodetector under ultraviolet light. Depletion regions are thinner but conduction channels are large, indicating larger current flow through tetrapods. (c) H_2 gas sensor structure in air at high temperatures and (d) gas sensor in H_2 gas; depletion regions or SCR are represented as more transparent zones. Conduction channels are through the middle part of tetrapods forming 3D networks.

DOI: 10.1021/acsami.5b02816
ACS Appl. Mater. Interfaces 2015, 7, 14303−14316

as can be seen from Figure 8c. According to eq 11, at temperatures lower than 100 °C the dominant adsorbed oxygen species is O_2^-. Under UV illumination, electron−hole (e^-, h^+) pairs are generated (eq 12) in ZnO tetrapods and release a captured electron back to the crystal. Generated holes interact with oxygen molecules ($O^-_{2(ads)}$), leading to desorption of oxygen from ZnO tetrapods (eq 13):[40,70]

$$h\nu \rightarrow h^+ + e^- \quad (12)$$

$$h^+ + O^-_{2(ads)} \rightarrow O_{2(g)} \quad (13)$$

As a result, according to eqs 12 and 13, the width of depletion zone SCR will decrease, the height of potential barriers between branches of tetrapods will be reduced (Figure 11b), and resistance of the sensor will be considerably declined (Figure 8c).[40]

The hydrogen gas sensing mechanism can be explained briefly as follows. For an example of ZnO in the detection of hydrogen, the following reaction (eq 14) may occur when the sample is placed in air[41] at relatively high temperatures:

$$O_2 + 2e^- \rightarrow 2O^-_{(ads)} \quad (14)$$

It should be noted that adsorbed oxygen may exist in multiple forms (see eq 11) with increasing temperature.[40,41] At high temperatures (in our case 400 °C), dominant species[40] are O_2^- and O^-, which are represented in Figure 11c by red spheres. In accordance with eq 14, after adsorption of the oxygen species, the SCR is created (Figure 11c). This form of tetrapods, especially due to long arms (sample set 2), results in the creation of many junctions between branches of ZnO-T. We can speculate that the H_2 gas molecules mainly play the role of reducing agents and donate electrons via the following reaction[40,41] (eq 15):

$$2O^-_{(ads)} + 2H_2 \rightarrow 2H_2O + 2e^- \quad (15)$$

Afterward, the reaction of hydrogen gas with adsorbed oxygen species on the surface of ZnO tetrapods will result in an increase of electrical current through structure (Figure 11d). It can be explained due to desorption of the adsorbed oxygen species from the surface of ZnO tetrapods, which will lead to the decrease of the depletion layer SCR width and, as a result, will increase the electrical current through the structure (Figure 11d; hydrogen molecules are represented by green double spheres). Gas-sensing mechanism can be attributed to (i) high porosity, due to the tetrapod form, that results in high surface-to-volume ratio at the tetrapod arm end and leads to improved gas response (hydrogen gas has a better diffusion ratio that results in improved response/recovery times); and (ii) more active centers, which represent junctions of the tetrapod core and the outer branches that are interconnected. Height of the potential barrier is modulated by donated electrons as a result of eq 13 (Figure 11b) in the case of UV detection and as a result of eq 15 in the case of hydrogen detection. Thus, a larger number of junctions between long and thin branches of tetrapods essentially improves hydrogen gas sensing and UV detection response.

4. CONCLUSIONS

In summary, ZnO tetrapods with different nanoarm morphologies forming interconnected macroscopic networks have been successfully fabricated via the flame transport synthesis process by controlling the technological regimes. The morphology of the tetrapods was found to be strongly dependent on the experimental parameters and precisely controlled, mainly by growth time (30−90 min) and temperature (900−950 °C) in air. It has been observed that, with progress in time, the shape of the tetrapods can be shifted in a controllable manner from uniform-shaped arms to sharp needle-type arms and finally a self-assembled interconnected macroscopic network of tetrapods. At higher temperatures, the growth of multipods is dominant over tetrapods. These tetrapods with different types of arm morphologies exhibit significantly high (over 95%) photocatalytic activity against methylene blue under UV irradiation, and for tetrapods with sharp needlelike arms, almost complete degradation of dye has been achieved in a very small time (∼10 min). A multifunctional device based on a network of ZnO tetrapods with sharp-needled arms was fabricated and utilized for UV photodetection. An increase in current value of more than 2 orders of magnitude ($I_{UVON}/I_{UVOFF} \approx 584$) for sensor structure with gap d = 100 μm and 1 order of magnitude ($I_{UVON}/I_{UVOFF} \approx 28$) for d = 1 mm has been detected for such sensors upon exposure to UV radiation. By increasing the postgrowth annealing time of ZnO-T networks before their integration into device structure, a higher response value has been obtained that is mainly due to better electron paths induced by stronger interconnections among arms of ZnO-T in the network. Another important point is that such structures show relatively fast rise/response time ($\tau_r \approx 40$ ms) and decay/recovery after the UV light is switched off. During H_2 gas exposure, a fast increase of the current value was detected, characterized by rapid rise/response time constants (rise time ∼80 ms, decay time ∼180 ms) for sensor structure (set 2) made from ZnO-T with elongated tips of the arms. The tetrapod structure formation mechanism and their UV-induced photocatalytic behaviors have been described in detail. For UV and gas-sensing mechanisms from the ZnO-T network device, a microscopic model has been proposed and has been thoroughly discussed. Presented results could be of great technological importance to understand ZnO-T growth by a rapid, effective, and controllable method, which can also be implemented in practice. This is an important step forward in technology for synthesis of macroscopic ZnO-T networks for lower power and faster zinc oxide tetrapod network-based nanosensing devices.

■ ASSOCIATED CONTENT

Supporting Information

Four figures showing high-resolution TEM studies on ZnO tetrapods, current ratio measured from sensor structures, and enhanced UV photocurrent response of device made of ZnO-T, and one table listing response and recovery times for three sets of ZnO-T based sensor structures. The Supporting Information is available free of charge on the ACS Publications website at DOI: 10.1021/acsami.5b02816.

■ AUTHOR INFORMATION

Corresponding Author

*E-mail ykm@tf.uni-kiel.de.

Notes

The authors declare no competing financial interest.

■ ACKNOWLEDGMENTS

We acknowledge support from the German Research Foundation (DFG) under the scheme PAK 902 (KI 1263/14-1 and AD 183/16-1). G.M. acknowledges the DAAD, Germany, for a fellowship under the DAAD-WISE program to work at University of Kiel. O.L. gratefully acknowledges the Alexander von Humboldt Foundation for the research fellowship for

DOI: 10.1021/acsami.5b02816
ACS Appl. Mater. Interfaces 2015, 7, 14303−14316

experienced researchers at the Institute for Materials Science, University of Kiel, Germany. This work was partially supported by the STCU within Grant 5989.

REFERENCES

(1) Hu, J.; Odom, T. W.; Lieber, C. M. Chemistry and Physics in One Dimension: Synthesis and Properties of Nanowires and Nanotubes. *Acc. Chem. Res.* **1999**, *32* (5), 435−445.
(2) Wang, Z. L. ZnO Nanowire and Nanobelt Platform for Nanotechnology. *Mater. Sci. Eng., R* **2009**, *64* (3−4), 33−71.
(3) Zeng, H.; Cai, W.; Liu, P.; Xu, X.; Zhou, H.; Klingshirn, C.; Kalt, H. ZnO-Based Hollow Nanoparticles by Selective Etching: Elimination and Reconstruction of Metal−Semiconductor Interface, Improvement of Blue Emission and Photocatalysis. *ACS Nano* **2008**, *2* (8), 1661−1670.
(4) Joshi, R. K.; Schneider, J. J. Assembly of One Dimensional Inorganic Nanostructures into Functional 2D and 3D Architectures. Synthesis, Arrangement and Functionality. *Chem. Soc. Rev.* **2012**, *41* (15), 5285−5312.
(5) Lupan, O.; Chow, L.; Chai, G.; Heinrich, H. Fabrication and Characterization of Zn−ZnO Core−shell Microspheres from Nanorods. *Chem. Phys. Lett.* **2008**, *465* (4), 249−253.
(6) Ostrikov, K.; Neyts, E. C.; Meyyappan, M. Plasma Nanoscience: From Nano-solids in Plasmas to Nano-plasmas in Solids. *Adv. Phys.* **2013**, *62* (2), 113−224.
(7) Xia, Y.; Rogers, J. A.; Paul, K. E.; Whitesides, G. M. Unconventional Methods for Fabricating and Patterning Nanostructures. *Chem. Rev.* **1999**, *99* (7), 1823−1848.
(8) Adelung, R.; Aktas, O. C.; Franc, J.; Biswas, A.; Kunz, R.; Elbahri, M.; Kanzow, J.; Schurmann, U.; Faupel, F. Strain-Controlled Growth of Nanowires within Thin-film Cracks. *Nat. Mater.* **2004**, *3* (6), 375−379.
(9) Gedamu, D.; Paulowicz, I.; Kaps, S.; Lupan, O.; Wille, S.; Haidarschin, G.; Mishra, Y. K.; Adelung, R. Rapid Fabrication Technique for Interpenetrated ZnO Nanotetrapod Networks for Fast UV Sensors. *Adv. Mater.* **2014**, *26* (10), 1541−1550.
(10) Reimer, T.; Paulowicz, I.; Röder, R.; Kaps, S.; Lupan, O.; Chemnitz, S.; Benecke, W.; Ronning, C.; Adelung, R.; Mishra, Y. K. Single Step Integration of ZnO Nano-and Microneedles in Si Trenches by Novel Flame Transport Approach: Whispering Gallery Modes and Photocatalytic Properties. *ACS Appl. Mater. Interfaces* **2014**, *6* (10), 7806−7815.
(11) Song, J.; Kulinich, S. A.; Yan, J.; Li, Z.; He, J.; Kan, C.; Zeng, H. Epitaxial ZnO Nanowire on Nanoplate Structures as Efficient and Transferable Field Emitters. *Adv. Mater.* **2013**, *25* (40), 5750−5755.
(12) Manna, L.; Milliron, D. J.; Meisel, A.; Scher, E. C.; Alivisatos, A. P. Controlled Growth of Tetrapod-branched Inorganic Nanocrystals. *Nat. Mater.* **2003**, *2* (6), 382−385.
(13) Chen, S.; Wang, Z. L.; Ballato, J.; Foulger, S. H.; Carroll, D. L. Monopod, Bipod, Tripod, and Tetrapod Gold Nanocrystals. *J. Am. Chem. Soc.* **2003**, *125* (52), 16186−16187.
(14) Choi, C. L.; Koski, K. J.; Olson, A. C. K.; Alivisatos, A. P. Luminescent Nanocrystal Stress Gauge. *Proc. Natl. Acad. Sci. U.S.A.* **2010**, *107* (50), 21306−21310.
(15) Wang, J.; Singh, A.; Liu, P.; Singh, S.; Coughlan, C.; Guo, Y.; Ryan, K. M. Colloidal Synthesis of Cu_2SnSe_3 Tetrapod Nanocrystals. *J. Am. Chem. Soc.* **2013**, *135* (21), 7835−7838.
(16) Zamani, R. R.; Ibáñez, M.; Luysberg, M.; García-Castelló, N.; Houben, L.; Prades, J. D.; Grillo, V.; Dunin-Borkowski, R. E.; Morante, J. R.; Cabot, A.; Arbiol, J. Polarity-Driven Polytypic Branching in Cu-Based Quaternary Chalcogenide Nanostructures. *ACS Nano* **2014**, *8* (3), 2290−2301.
(17) Mishra, Y. K.; Kaps, S.; Schuchardt, A.; Paulowicz, I.; Jin, X.; Gedamu, D.; Wille, S.; Lupan, O.; Adelung, R. Versatile Fabrication of Complex Shaped Metal Oxide Nano-microstructures and Their Interconnected Networks for Multifunctional Applications. *KONA Powder Part. J.* **2014**, *31*, 92−110.
(18) Shi, J.; Grutzik, S.; Wang, X. Zn Cluster Drifting Effect for the Formation of ZnO 3D Nanoarchitecture. *ACS Nano* **2009**, *3* (6), 1594−1602.
(19) Lao, J. Y.; Wen, J. G.; Ren, Z. F. Hierarchical ZnO Nanostructures. *Nano Lett.* **2002**, *2* (11), 1287−1291.
(20) Tian, Z. R.; Voigt, J. A.; Liu, J.; McKenzie, B.; McDermott, M. J.; Rodriguez, M. A.; Konishi, H.; Xu, H. Complex and Oriented ZnO Nanostructures. *Nat. Mater.* **2003**, *2* (12), 821−826.
(21) Tsivion, D.; Schvartzman, M.; Popovitz-Biro, R.; Joselevich, E. Guided Growth of Horizontal ZnO Nanowires with Controlled Orientations on Flat and Faceted Sapphire Surfaces. *ACS Nano* **2012**, *6* (7), 6433−6445.
(22) Mills, A.; Davies, R. H.; Worsley, D. Water Purification by Semiconductor Photocatalysis. *Chem. Soc. Rev.* **1993**, *22* (6), 417−425.
(23) Shen, W.; Li, Z.; Wang, H.; Liu, Y.; Guo, Q.; Zhang, Y. Photocatalytic Degradation for Methylene Blue Using Zinc Oxide Prepared by Codeposition and Sol−gel Methods. *J. Hazard. Mater.* **2008**, *152* (1), 172−175.
(24) Wang, J.; Wang, Z.; Huang, B.; Ma, Y.; Liu, Y.; Qin, X.; Zhang, X.; Dai, Y. Oxygen Vacancy Induced Band-Gap Narrowing and Enhanced Visible Light Photocatalytic Activity of ZnO. *ACS Appl. Mater. Interfaces* **2012**, *4* (8), 4024−4030.
(25) Qin, H.; Li, W.; Xia, Y.; He, T. Photocatalytic Activity of Heterostructures Based on ZnO and N-Doped ZnO. *ACS Appl. Mater. Interfaces* **2011**, *3* (8), 3152−3156.
(26) Wang, X.; Liu, W.; Liu, J.; Wang, F.; Kong, J.; Qiu, S.; He, C.; Luan, L. Synthesis of Nestlike ZnO Hierarchically Porous Structures and Analysis of Their Gas Sensing Properties. *ACS Appl. Mater. Interfaces* **2012**, *4* (2), 817−825.
(27) Park, S.; An, S.; Ko, H.; Jin, C.; Lee, C. Synthesis of Nanograined ZnO Nanowires and Their Enhanced Gas Sensing Properties. *ACS Appl. Mater. Interfaces* **2012**, *4* (7), 3650−3656.
(28) Wong, K. K.; Ng, A.; Chen, X. Y.; Ng, Y. H.; Leung, Y. H.; Ho, K. H.; Djurišić, A. B.; Ng, A. M. C.; Chan, W. K.; Yu, L.; Phillips, D. L. Effect of ZnO Nanoparticle Properties on Dye-Sensitized Solar Cell Performance. *ACS Appl. Mater. Interfaces* **2012**, *4* (3), 1254−1261.
(29) Jiang, W.-T.; Wu, C.-T.; Sung, Y.-H.; Wu, J.-J. Room-Temperature Fast Construction of Outperformed ZnO Nanoarchitectures on Nanowire-Array Templates for Dye-Sensitized Solar Cells. *ACS Appl. Mater. Interfaces* **2013**, *5* (3), 911−917.
(30) Hu, W.; Liu, Y.; Yang, H.; Zhou, X.; Li, C. M. ZnO Nanorods-enhanced Fluorescence for Sensitive Microarray Detection of Cancers in Serum without Additional Reporter-amplification. *Biosens. Bioelectron.* **2011**, *26* (8), 3683−3687.
(31) Wahab, R.; Dwivedi, S.; Umar, A.; Singh, S.; Hwang, I.; Shin, H.-S.; Musarrat, J.; Al-Khedhairy, A. A.; Kim, Y.-S. ZnO Nanoparticles Induce Oxidative Stress in Cloudman S91 Melanoma Cancer Cells. *J. Biomed. Nanotechnol.* **2013**, *9* (3), 441−449.
(32) Mishra, Y. K.; Kaps, S.; Schuchardt, A.; Paulowicz, I.; Jin, X.; Gedamu, D.; Freitag, S.; Claus, M.; Wille, S.; Kovalev, A.; Gorb, S. N.; Adelung, R. Fabrication of Macroscopically Flexible and Highly Porous 3D Semiconductor Networks from Interpenetrating Nanostructures by a Simple Flame Transport Approach. *Part. Part. Syst. Charact.* **2013**, *30* (9), 775−783.
(33) Mecklenburg, M.; Schuchardt, A.; Mishra, Y. K.; Kaps, S.; Adelung, R.; Lotnyk, A.; Kienle, L.; Schulte, K. Aerographite: Ultra Lightweight, Flexible Nanowall, Carbon Microtube Material with Outstanding Mechanical Performance. *Adv. Mater.* **2012**, *24* (26), 3486−3490.
(34) Schuchardt, A.; Braniste, T.; Mishra, Y. K.; Deng, M.; Mecklenburg, M.; Stevens-Kalceff, M. A.; Raevschi, S.; Schulte, K.; Kienle, L.; Adelung, R.; Tiginyanu, I. Three-dimensional Aerographite-GaN Hybrid Networks: Single Step Fabrication of Porous and Mechanically Flexible Materials for Multifunctional Applications. *Sci. Rep.* **2015**, *5*, 8839.
(35) Stadelmann, P. A. EMS: A Software Package for Electron Diffraction Analysis and HREM Image Simulation in Materials Science. *Ultramicroscopy* **1987**, *21* (2), 131−145.
(36) Hrkac, V.; Kienle, L.; Kaps, S.; Lotnyk, A.; Mishra, Y. K.; Schurmann, U.; Duppel, V.; Lotsch, B. V.; Adelung, R. Superposition Twinning Supported by Texture in ZnO Nanospikes. *J. Appl. Crystallogr.* **2013**, *46* (2), 396−403.

DOI: 10.1021/acsami.5b02816
ACS Appl. Mater. Interfaces 2015, 7, 14303−14316

(37) Kilaas, R. Optimal and Near-optimal Filters in High-resolution Electron Microscopy. *J. Microsc.* **1998**, *190* (1−2), 45−51.
(38) Robinson, J. W. *Atomic Spectroscopy*; CRC Press: Boca Raton, FL, 1996.
(39) Xie, J.; Wang, H.; Duan, M.; Zhang, L. Synthesis and Photocatalysis Properties of ZnO Structures with Different Morphologies via Hydrothermal Method. *Appl. Surf. Sci.* **2011**, *257* (15), 6358−6363.
(40) Lupan, O.; Chow, L.; Chai, G. A Single ZnO Tetrapod-based Sensor. *Sens. Actuators, B* **2009**, *141* (2), 511−517.
(41) Lupan, O.; Ursaki, V. V.; Chai, G.; Chow, L.; Emelchenko, G. A.; Tiginyanu, I. M.; Gruzintsev, A. N.; Redkin, A. N. Selective Hydrogen Gas Nanosensor using Individual ZnO Nanowire with Fast Response at Room Temperature. *Sens. Actuators, B* **2010**, *144* (1), 56−66.
(42) Fan, Z.; Lu, J. G. Zinc Oxide Nanostructures: Synthesis and Properties. *J. Nanosci. Nanotechnol.* **2005**, *5* (10), 1561−1573.
(43) Lim, Y.; Park, J.; Hong, S.-T.; Kim, J. Carbothermal Synthesis of ZnO Nanocomb Structure. *Mater. Sci. Eng., B* **2006**, *129* (1), 100−103.
(44) Hejazi, S.; Hosseini, H.; Ghamsari, M. S. The Role of Reactants and Droplet Interfaces on Nucleation and Growth of ZnO Nanorods Synthesized by Vapor−liquid−solid (VLS) Mechanism. *J. Alloys Compd.* **2008**, *455* (1), 353−357.
(45) Li, W.-J.; Shi, E.-W.; Zhong, W.-Z.; Yin, Z.-W. Growth Mechanism and Growth Habit of Oxide Crystals. *J. Cryst. Growth* **1999**, *203* (1), 186−196.
(46) Ye, C.; Fang, X.; Hao, Y.; Teng, X.; Zhang, L. Zinc Oxide Nanostructures: Morphology Derivation and Evolution. *J. Phys. Chem. B* **2005**, *109* (42), 19758−19765.
(47) Song, R. Q.; Xu, A. W.; Deng, B.; Li, Q.; Chen, G. Y. From Layered Basic Zinc Acetate Nanobelts to Hierarchical Zinc Oxide Nanostructures and Porous Zinc Oxide Nanobelts. *Adv. Funct. Mater.* **2007**, *17* (2), 296−306.
(48) Zheng, K.; Xu, C.; Zhu, G.; Li, X.; Liu, J.; Yang, Y.; Sun, X. Formation of Tetrapod and Multipod ZnO Whiskers. *Physica E (Amsterdam, Neth.)* **2008**, *40* (8), 2677−2681.
(49) Dai, Y.; Zhang, Y.; Li, Q.; Nan, C. Synthesis and Optical Properties of Tetrapod-like Zinc Oxide Nanorods. *Chem. Phys. Lett.* **2002**, *358* (1), 83−86.
(50) Shiojiri, M.; Kaito, C. Structure and Growth of ZnO Smoke Particles Prepared by Gas Evaporation Technique. *J. Cryst. Growth* **1981**, *52*, 173−177.
(51) Nishio, K.; Isshiki, T.; Kitano, M.; Shiojiri, M. Structure and Growth Mechanism of Tetrapod-like ZnO Particles. *Philos. Mag. A* **1997**, *76* (4), 889−904.
(52) Takeuchi, S.; Iwanaga, H.; Fujii, M. Octahedral Multiple-twin Model of Tetrapod ZnO Crystals. *Philos. Mag. A* **1994**, *69* (6), 1125−1129.
(53) Dai, Y.; Zhang, Y.; Wang, Z. L. The Octa-twin Tetraleg ZnO Nanostructures. *Solid State Commun.* **2003**, *126* (11), 629−633.
(54) Ronning, C.; Shang, N. G.; Gerhards, I.; Hofsäss, H.; Seibt, M. Nucleation Mechanism of the Seed of Tetrapod ZnO Nanostructures. *J. Appl. Phys.* **2005**, *98* (3), No. 034307.
(55) Iwanaga, H.; Fujii, M.; Ichihara, M.; Takeuchi, S. Some Evidence for the Octa-twin Model of Tetrapod ZnO Particles. *J. Cryst. Growth* **1994**, *141* (1), 234−238.
(56) Yan, H.; He, R.; Pham, J.; Yang, P. Morphogenesis of One-dimensional ZnO Nano- and Microcrystals. *Adv. Mater.* **2003**, *15* (5), 402−405.
(57) Seo, J.; Kuk, S.; Kim, K. Thermal Decomposition of PVB (Polyvinyl Butyral) Binder in the Matrix and Electrolyte of Molten Carbonate Fuel Cells. *J. Power Sources* **1997**, *69* (1), 61−68.
(58) Lide, D.; Haynes, W. *CRC Handbook of Chemistry and Physics: A Ready-reference Book of Chemical and Physical Data*. CRC Press: Boca Raton, FL, 2009.
(59) Gaskell, D. R. *Introduction to the Thermodynamics of Materials*; CRC Press: Boca Raton, FL, 2008; Vol. 2.
(60) Chow, L.; Lupan, O.; Chai, G.; Khallaf, H.; Ono, L.; Roldan Cuenya, B.; Tiginyanu, I.; Ursaki, V.; Sontea, V.; Schulte, A. Synthesis and Characterization of Cu-doped ZnO One-dimensional Structures for Miniaturized Sensor Applications with Faster Response. *Sens. Actuators, A* **2013**, *189*, 399−408.
(61) Lupan, O.; Chow, L.; Ono, L. K.; Cuenya, B. R.; Chai, G.; Khallaf, H.; Park, S.; Schulte, A. Synthesis and Characterization of Ag-or Sb-doped ZnO Nanorods by a Facile Hydrothermal Route. *J. Phys. Chem. C* **2010**, *114* (29), 12401−12408.
(62) Ding, Y.; Wang, Z. L. Structures of Planar Defects in ZnO Nanobelts and Nanowires. *Micron* **2009**, *40* (3), 335−342.
(63) Liqiang, J.; Yichun, Q.; Baiqi, W.; Shudan, L.; Baojiang, J.; Libin, Y.; Wei, F.; Honggang, F.; Jiazhong, S. Review of Photoluminescence Performance of Nano-sized Semiconductor Materials and its Relationships with Photocatalytic Activity. *Sol. Energy Mater. Sol. Cells* **2006**, *90* (12), 1773−1787.
(64) Augugliaro, V.; Bellardita, M.; Loddo, V.; Palmisano, G.; Palmisano, L.; Yurdakal, S. Overview on Oxidation Mechanisms of Organic Compounds by TiO_2 in Heterogeneous Photocatalysis. *J. Photochem. Photobiol., C* **2012**, *13* (3), 224−245.
(65) Li, D.; Haneda, H. Morphologies of Zinc Oxide Particles and Their Effects on Photocatalysis. *Chemosphere* **2003**, *51* (2), 129−137.
(66) McLaren, A.; Valdes-Solis, T.; Li, G.; Tsang, S. C. Shape and Size Effects of ZnO Nanocrystals on Photocatalytic Activity. *J. Am. Chem. Soc.* **2009**, *131* (35), 12540−12541.
(67) Guo, M. Y.; Ng, A. M. C.; Liu, F.; Djurišić, A. B.; Chan, W. K.; Su, H.; Wong, K. S. Effect of Native Defects on Photocatalytic Properties of ZnO. *J. Phys. Chem. C* **2011**, *115* (22), 11095−11101.
(68) Parida, K. M.; Dash, S. S.; Das, D. P. Physico-chemical Characterization and Photocatalytic Activity of Zinc Oxide Prepared by Various Methods. *J. Colloid Interface Sci.* **2006**, *298* (2), 787−793.
(69) Farbod, M.; Jafarpoor, E. Hydrothermal Synthesis of Different Colors and Morphologies of ZnO Nanostructures and Comparison of Their Photocatalytic Properties. *Ceram. Int.* **2014**, *40* (5), 6605−6610.
(70) Chai, G.; Lupan, O.; Chow, L.; Heinrich, H. Crossed Zinc Oxide Nanorods for Ultraviolet Radiation Detection. *Sens. Actuators, A* **2009**, *150* (2), 184−187.

DOI: 10.1021/acsami.5b02816
ACS Appl. Mater. Interfaces 2015, 7, 14303−14316